



# Modeling earthquake sequences along the Manila subduction zone: Effects of three-dimensional fault geometry

Hongyu Yu<sup>a,b,\*</sup>, Yajing Liu<sup>a</sup>, Hongfeng Yang<sup>c</sup>, Jieyuan Ning<sup>d</sup>

<sup>a</sup> Department of Earth and Planetary Sciences, McGill University, Montréal, Québec, Canada

<sup>b</sup> Institut für Geologie, Mineralogie und Geophysik, Ruhr-Universität Bochum, Bochum, Germany

<sup>c</sup> Earth System Science Programme, Chinese University of Hong Kong, Hong Kong, China

<sup>d</sup> School of Earth and Space Sciences, Peking University, Beijing, China

## ARTICLE INFO

### Keywords:

Large-scale fault geometrical effect  
3D earthquake cycle modeling  
Manila trench  
Seismic hazard assessment

## ABSTRACT

To assess the potential of catastrophic megathrust earthquakes ( $M_W > 8$ ) along the Manila Trench, the eastern boundary of the South China Sea, we incorporate a 3D non-planar fault geometry in the framework of rate-state friction to simulate earthquake rupture sequences along the fault segment between 15°N–19°N of northern Luzon. Our simulation results demonstrate that the first-order fault geometry heterogeneity, the transitional-segment (possibly related to the subducting Scarborough seamount chain) connecting the steeper south segment and the flatter north segment, controls earthquake rupture behaviors. The strong along-strike curvature at the transitional-segment typically leads to partial ruptures of  $M_W \sim 8.3$  and  $M_W \sim 7.8$  along the southern and northern segments respectively. The entire fault occasionally ruptures in  $M_W \sim 8.8$  events when the cumulative stress in the transitional-segment is sufficiently high to overcome the geometrical inhibition. Fault shear stress evolution, represented by the  $S$ -ratio, is clearly modulated by the width of seismogenic zone ( $W$ ). At a constant plate convergence rate, a larger  $W$  indicates on average lower interseismic stress loading rate and longer rupture recurrence period, and could slow down or sometimes stop ruptures that initiated from a narrower portion. Moreover, the modeled interseismic slip rate before whole-fault rupture events is comparable with the coupling state that was inferred from the interplate seismicity distribution, suggesting the Manila trench could potentially rupture in a  $M8+$  earthquake.

## 1. Introduction

The largest earthquakes in the world mostly occur in shallow part of subduction zones, sometimes accompanied by strong tsunami waves, causing catastrophic damages in the source areas and along the near-field coastlines. For regions with frequently occurring large earthquakes such as Chile, Nankai, Sumatra, a variety of studies have investigated the properties of the subduction zone faults so as to better evaluate the future megathrust rupture potential (e.g. Lay, 2015; Yin et al., 2016). In contrast, subduction zones with no historical records of large earthquakes have received less attention, partly due to the lack of observational data. For example, at a fast convergence rate of  $\sim 7$  cm/yr between the Philippine Sea Plate and the Sunda/Eurasian Plate from offshore Taiwan to northern Luzon of Philippines (Fig. 1), the Manila Trench has hosted numerous earthquakes with small to moderate magnitudes (Bautista and Oike, 2000). However, large earthquakes are infrequent as indicated by modern observations (Fig. 1); the maximum magnitude being  $M7.8$  since 1560s (Repetti, 1946). In particular,

$M > 6$  earthquakes have rarely been recorded along the northern trench. The lack of large earthquakes may indicate the subduction fault is either aseismically slipping or is accumulating strain energy toward rapid release in a future megathrust event. Moreover, Chinese historical records indicate that a possible tsunami event in 1076 CE had inundated about 500 km of the southeast China coastline, and might have been generated by a megathrust earthquake along the Manila trench (Yang and Wei, 2005; Megawati et al., 2009). As the eastern tectonic boundary of the South China Sea, a Manila megathrust earthquake could cause devastating tsunami waves thus endanger tens of millions of population residing along the west coast of the Luzon Island, Taiwan and southeast China (Megawati et al., 2009; Wu and Huang, 2009). However, the current Manila tsunami scenario models are poorly constrained due to the absence of reliable rupture models (Megawati et al., 2009; Liu et al., 2007; Liu et al., 2009). Therefore, it is of critical importance to quantitatively evaluate the seismogenic potential for the Manila subduction zone.

The state of interseismic coupling between the subducting plate and

\* Corresponding author at: Institut für Geologie, Mineralogie und Geophysik, Ruhr-Universität Bochum, Bochum, Germany.  
E-mail address: [hongyu.yu@mail.mcgill.ca](mailto:hongyu.yu@mail.mcgill.ca) (H. Yu).

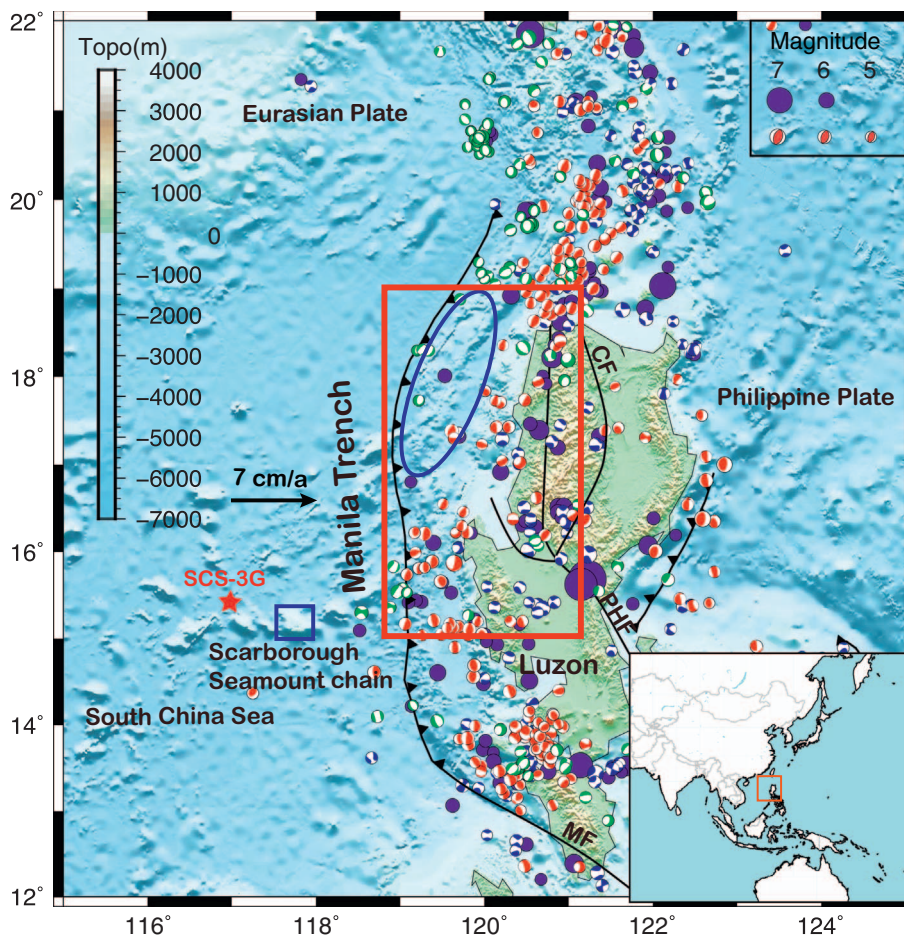


Fig. 1. Earthquakes and tectonic settings of the Manila subduction zone. A total of 540 focal mechanism solutions from the GCMT catalog during 1976–2013 are classified into three groups: thrust-faulting events (red), normal-faulting events (green), and strike-slip events (blue). Earthquakes ( $M_6+$ ) reported by the International Seismological Centre (ISC) during 1970/01/01–2016/01/01 are marked as solid circles (purple). Red rectangle: model simulation area. Blue ellipse: area of low seismicity rate. Blue rectangle: Scarborough Shoal. Star: IODP Expedition 349 (South China Sea), site U1431 (SCS-3G). PF: Philippine Fault. CF: Cagayan Fault. MF: Mindoro Fault. Fault traces are modified from *Fan and Wu (2014)*. (For interpretation of the references to color in this figure legend, the reader is referred to the web version of this article.)

the overlying plate is commonly used as an indication for the seismic potential of  $M_8$  megathrust earthquakes in global subduction zones (Miller et al., 2001; Nishimura et al., 2004; Reyners, 1998; Kaneko et al., 2010). However, the small number of GPS stations (~50 campaign-mode Luzon sites and 15 permanent IGS sites in Asia-Pacific) (Yu et al., 1999; Galgana et al., 2007), the short instrumentation history (since 1995) and the limited understanding of the regional tectonic setting jointly result in a poor constraint of the plate coupling of the Manila subduction zone, especially near the trench (Galgana et al., 2007; Hsu et al., 2012; McCaffrey, 2002; Wang and Tréhu, 2016). The current estimate of interseismic locking distribution varies among different geodetic inversion models. Galgana et al. (2007) used a 6-mobile-elastic-block model and found the Manila Trench to be 100% free sliding (or, 0% locking) based on observations from 52 campaign GPS stations in Luzon during 1996–2002. Hsu et al. (2012) estimated an average coupling ratio of 0.4 based on a combined dataset of permanent and campaign GPS observations during 1996–2008, trench-parallel gravity anomalies, and seafloor bathymetry. They also suggested that partial locking at  $15^\circ\text{N}$ – $16.5^\circ\text{N}$  may be attributed to the subduction of the Scarborough Seamount Chain (SSC), and may indicate aseismic slip. The difference between the coupling ratio estimates of the above two studies is likely due to the different treatments of the upper plate deformation, instead of the use of different GPS data (Wang and Bilek, 2014). More recently, Hsu et al. (2016) inferred that the accumulated strain along the  $15^\circ\text{N}$ – $19^\circ\text{N}$  segment could be equivalent to an  $M_w$  8.8–9.2 earthquake with a 500 to 1000-year recurrence interval, respectively, based on the inversion of 31 continuous GPS sites from 1998 to 2015 using two types of block models. In addition to the large discrepancies displayed by various geodetic inversion models, a low plate coupling ratio alone does not necessarily imply low risk of megathrust

rupture. A modern-day example is the 2011  $M_9$  Tohoku-Oki earthquake. Its unprecedented large coseismic slip near the trench was not predicted by any of the interplate coupling models based on GPS observations (Scholz and Campos, 2012, and references therein). Sparse geodetic instrumentation, lack of knowledge for block rotation and possible temporal variations in the plate coupling state could all have contributed to the seemingly contradictory understandings. Based on the incomplete observation history, we cannot rule out the possibility of any subduction zone generating an  $M_8+$  earthquake (McCaffrey, 2008). Thus, it is necessary to take caution in seismic hazard assessment for the Manila Trench.

As highlighted in Fig. 1, earthquake distribution within our study area is clearly segmented around  $16^\circ\text{N}$ – $17^\circ\text{N}$ , with most interplate earthquakes as far as 100–200 km from the trench to the north and nearly all clustered within 100 km from the trench to the south. The seismicity segmentation has been hypothesized to be related to the subduction of the Scarborough Seamount Chain (SSC), coincidentally around  $16^\circ\text{N}$ – $17^\circ\text{N}$ . The presence of subducted SSC may have contributed to much greater subduction fault dipping angles to the south and steep along-strike gradient within the north-south transition at  $16^\circ\text{N}$ – $17^\circ\text{N}$  (Bautista et al., 2001). While this along-strike segmentation in seismicity may be obvious from the current catalog consisting earthquakes of magnitudes up to 7, it is unclear whether the pattern is persistent if  $M_8$  or greater earthquakes occur along the Manila Trench. Recent studies have suggested subducting seamounts can terminate earthquake ruptures (Yang et al., 2012, 2013), and rough topography of the incoming seafloor is correlated with subduction margins lack of  $M_8+$  great earthquakes (Wang and Bilek, 2014). These are consistent with the recent report that large curvatures in the shape of the subduction slab can increase shear strength heterogeneity and hence

inhibit the occurrences of larger earthquakes (Bletery et al., 2016). King (1986) has discussed the first-order 3D geometrical effects on along-depth and along-strike rupture propagation for dip-slip and strike-slip earthquakes, respectively. He suggested that a fault bending geometry could serve as a barrier in terminating the coseismic rupture, or act as an asperity to initiate a future earthquake, depending on the slip deficit there. To summarize, the correlations in the previous studies are made from observations of global subduction zones and tested with simplified analytical or two-dimensional numerical models. The influence of the large-scale variation of three-dimensional fault geometry on along-strike rupture propagation of megathrust earthquakes has not yet been thoroughly quantified for individual rupture events in individual subduction zones.

In this study, we take a numerical modeling approach to quantitatively investigate the seismogenic potential of megathrust earthquakes along the Manila Trench. In particular, we focus on the influence of subduction slab geometry on earthquake rupture patterns in northern Luzon. We build a 3D Manila subduction fault model with geometry constrained by seismicity hypocenters to simulate earthquake sequences and rupture patterns. Based on Li and Liu (2016), we developed codes to model earthquake sequences on a 3D nonplanar fault. The implementation of the laboratory-derived rate- and state-dependent friction law in the 3D model allows us to simulate multiple earthquake sequences, including interseismic strain accumulation, earthquake nucleation, rupture propagation and afterslip behaviors on the fault (Lapusta and Rice, 2003). The physics-based modeling approach also allows us to quantify the degree of plate coupling and assess stress state conditions favorable or prohibitive for earthquake nucleation and rupture propagation, and renders the possibility to identify a snapshot in the modeled earthquake cycle consistent with observed interplate seismicity, and infer for megathrust rupture and tsunami potential along the coast of the South China Sea.

## 2. Model setup

In this section, we introduce how we construct the subduction fault geometry and apply the rate-state friction law and constitutive relations in the simulation. We also describe the choices of friction parameters, triangular mesh generation, and model resolution tests to satisfy the requirements dictated by the constitutive equations as well as computational resources.

### 2.1. Slab geometry and model mesh generation

We construct the subducting Sunda/Eurasian slab geometry between 15°N and 19°N based on distribution of seismicity compiled by Bautista et al. (2001) and this study. In total, 7895 earthquake hypocenters (1970/01/01 to 2014/01/01) reported by the International Seismological Centre (ISC) are used to constrain the geometry of the subduction fault, as shown in the Supplementary Fig. S1 for five depth cross-sections along the trench. Both the earthquake hypocenters (Fig. S1) and focal mechanism solutions (Bautista et al., 2001) indicate the fault dipping angle gradually changes from ~37° south of the Scarborough Seamount Chain (SSC) to ~15° north of it down to ~60 km into the upper mantle. We further extrapolate the spline-fitted fault geometry to a continuously curved fault model, and use the bathymetry to depict the along-strike shape of the trench (Fig. 1). As shown in Fig. 2(a), our model extends 272 km and 450 km in the trench-normal (x-axis) and trench-parallel (y-axis) directions, respectively, equivalent to 60 km in the vertical depth (z-axis). As the curved slab model inferred from interplate seismicity reflects the large-scale fault geometry variation but does not explicitly include the topographic features of the subducted SSC, this study focuses on the effects of along-strike variation of the megathrust dip angle rather than the role of seamount chain on fault slip history. We will refer to the segment at 16°N–17°N with the steepest along-strike gradient in topography as a transitional-segment.

To better describe the non-planar fault geometry, we use an unstructured mesh composed of triangular elements to discretize the fault surface, following Shibasaki et al. (2012) and Li and Liu (2016). We first generate a uniform rectangular grid with GMT (Wessel and Bercovici, 1998), then pair neighbor nodes into edges (edges and diagonals of the rectangular grids), and further combine these edges into triangular grids. The geometry of any individual element on the fault is fully described by its local dip angle  $\phi$  and local strike angle  $\psi$ , which are separately defined as the angle between the element and x-/y-axis. As illustrated in Fig. 2(a), for an element with a normal direction of  $\vec{n}$ , the local dip  $\phi$  and the local strike  $\psi$  are respectively the complementary angles of  $n_{xz}$  from x-axis and  $n_{yz}$  from y-axis, where  $n_{xz}$  and  $n_{yz}$  are denoted as the projection of  $\vec{n}$  onto the x-z plane and y-z plane, separately. An element tilting to south has a positive local strike angle. The change in dip angle and the curved trench shape jointly lead to the complexity of the local strike distribution. There are three areas of negative local strikes, i.e., the down-dip parts toward the southern and northern boundaries of the model domain sides and the up-dip 10 km of the along-strike transition (~200–320 km) (Fig. S2).

### 2.2. Constitutive equations and parameters

In the framework of rate- and state-dependent friction law (Dieterich, 1979; Ruina, 1983), friction coefficient is dependent on the fault slip rate  $V$  and slip history, represented by the variation of state variable  $\theta$ ,

$$\tau = \bar{\sigma} \left[ f_0 + a \ln \left( \frac{V}{V_0} \right) + b \ln \left( \frac{V_0 \theta}{d_c} \right) \right]. \quad (1)$$

We use the “ageing” version of state variable ( $\theta$ ) evolution law,

$$\frac{d\theta}{dt} = 1 - \frac{V\theta}{d_c}. \quad (2)$$

Here  $\tau$  is shear stress and  $\bar{\sigma}$  is effective normal stress, defined as the difference between normal stress and pore pressure. The setting of a constant effective normal stress is based on the assumption of fluid over-pressurization at depths, as suggested for global subduction zones (Saffer and Tobin, 2011). Specifically, we set  $\bar{\sigma} = \min(2.8 + 18 * z, 50) \text{ MPa}$  ( $z$  is vertical depth in km) (Rice, 1992). The simplified constant and uniform  $\bar{\sigma}$  might underestimate the effect of stress concentration and hence the amount of coseismic slip at segments of steep topographic gradient (e.g., at 16°N–17°N along the strike), and the effect may be more significant under a fully dynamic case (Thomas et al., 2014). Nevertheless, our goal here is to discuss the effects of first-order geometrical features (on the scale of ~100 km) on along-strike rupture propagating behaviors and our modeling result is to certain extent valid for the discussion of this topic. The implications of using a constant effective normal stress will be discussed in more detail in Section 4.1. We follow Liu and Rice (2009) to adopt the laboratory measurement of friction stability parameter  $a$ - $b$  for gabbro gouges under hydrothermal conditions (He et al., 2007), and convert the temperature-dependent friction stability parameter  $a$ - $b$  to depth-dependent using a Manila subduction zone thermal model (Fig. S3a) (Gao et al., 2012). As shown in Fig. S3b, the rate-state velocity-weakening zone (where  $a$ - $b$  < 0, also termed “seismogenic zone”) is located between vertical depths of 2 and 42 km, and coincides with the depth range of low seismicity rate (Fig. 2b). This spatial correlation will be further discussed in Section 4 in the context of plate coupling state. Since we consider the  $a$ - $b$  as depth dependent, the seismogenic width  $W$  here is inversely proportional to the sine of the dip angle. That is, the along-strike variation of  $W$  is dependent on the dip angle variation in our model, although the realistic distribution of a seismogenic zone could be more complex (Wang and Tréhu, 2016). A complete list of friction parameters and values used in the simulation is presented in Table 1.

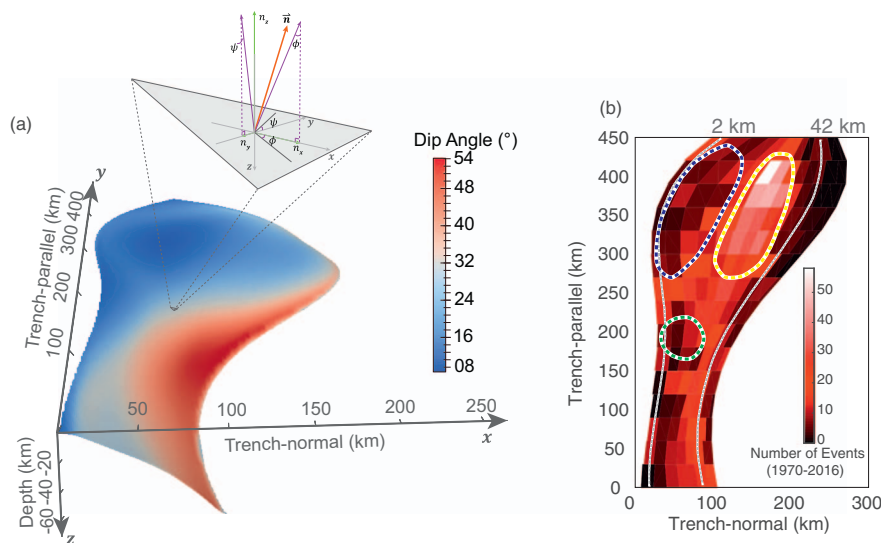


**Fig. 2.** (a) 3D Curved fault geometry. The reference point is (119.16°E,15.00°N). Color represents local dip angle of each grid element. One of the elements is zoomed in to show the sketch of local dip/strike angles. (b) Distribution of interplate seismicity, using 1763 earthquakes within 15 km to the slab interface from the ISC catalog, 1970–2016. Color indicates earthquake number in each grid. Blue and green dashed circles: seismically quiet area; Yellow dashed circle: seismically active area. Grey dashed lines depict the depth contours of 2 km and 42 km, respectively, as the upper and lower limits of the modeled seismogenic zone. (For interpretation of the references to color in this figure legend, the reader is referred to the web version of this article.)

**Table 1**

Summary of parameters used in 3D curved fault modeling. Friction stability parameter ( $\alpha$ - $b$ ) is presented in Fig. S3.

Steady state friction coefficient at $V_0$	$f_0$	0.6
Reference velocity	$V_0$	1 $\mu\text{m/s}$
Characteristic slip distance	$d_c$	34.4 mm
Shear modulus	$\mu$	30 GPa
Poisson's ratio	$\nu$	0.25
Characteristic nucleation size	$h^*$	5 km
Grid size	$h$	1 km
Coseismic velocity threshold	$V_{thres}$	5 mm/s
Plate convergence rate	$V_{pl}$	70 mm/year
Rate parameter	$\alpha$	0.01

We adopt the quasi-dynamic approximation of the elastic relation between the down-dip slip ( $\delta$ ) and the shear stress ( $\tau$ ) on the fault,

$$\tau_i(t) = \tau_0 - \sum_{j=1}^N k_{i,j} [\delta_j(t) - V_{pl}t] - \eta \frac{\partial \delta_i(t)}{\partial t}, \quad (3)$$

where subscripts  $i, j$  denote model grid indexes. The stiffness matrix  $k_{i,j}$  represents the shear stress change on cell  $i$  due to a unit down-dip dislocation on cell  $j$ , which is calculated for a homogeneous elastic half-space model with triangular elements (Okada, 1992; Stuart et al., 1997). Hsu et al. (2016) estimated the plate convergence rate and seismic slip rate along the 15°N–19°N segment of Manila Trench based on GPS observations and seismic activity, respectively, and further obtained the slip deficit rate as 67–73 mm/yr with an oblique angle of  $\sim 8^\circ$  by reducing seismic slip rate from the plate convergence rate. Taking into account that under the framework of rate and state friction, almost all the plate convergence would turn into slip deficit (full locking) and be released coseismically within the seismogenic zone ( $\alpha$ - $b < 0$ ). Therefore, we uniformly set the plate convergence rate  $V_{pl}$  as 70 mm/yr along the down-dip direction. This simplification on our non-planar fault model may result in a slower interseismic stress loading rate at the transitional-segment, and hence slightly underestimate its strain energy during the interseismic period, which could artificially strengthen the inhibition of rupture propagating from the southern segment to the north, or make it less prone to nucleate an earthquake there.  $\eta$  is a damping factor introduced to avoid unbounded slip rate during coseismic rupture (Rice, 1993). Here we set  $\eta = \mu/2c_s$ , where  $\mu$  is shear modulus and  $c_s$  is shear wave velocity. The quasi-dynamic approximation would result in slower rupture propagation, smaller slip rates and slip distance, while the rupture area and earthquake intervals are still comparable to those from fully dynamic simulations (Lapusta

and Rice, 2003). However, we note that such qualitative comparisons may be different when more heterogeneous velocity-weakening patches are included in the model, especially if additional coseismic weakening effects are considered (Thomas et al., 2014).

The initial conditions ( $t = 0$ ) are set to be close to steady state,  $V(x, \xi, 0) = V_{pl}$ , and  $\theta(x, \xi, 0) = \frac{d_c(x, \xi)}{1.1V(x, \xi, 0)}$  in all simulation cases. The slip deficits ( $\delta(t) - V_{pl}t$ ) at the fault boundaries are set to be zero, so that they will not load the model area.

### 2.3. Grid size

The characteristic earthquake nucleation size is the minimum dimension on the fault that would lead to a seismic rupture, defined as  $h^* = \frac{2\mu d_c}{\pi(1-\nu)(b-a)\bar{\sigma}}$  (Rice, 1993; Lapusta et al., 2000). As the slip evolution distance  $d_c$  is on the order of tens of microns from laboratory experiments (e.g., Blanpied et al., 1995), the corresponding nucleation size would be of several meters if we use  $a$ - $b$  and  $\bar{\sigma}$  values assumed above, which in turn requires an extremely small grid size in order to satisfy the continuum requirement in the simulation of earthquake sequences (Lapusta and Rice, 2003). The computational demand would be too much for the model dimension of hundreds of kilometers in this study. Therefore, we follow previous studies to choose  $d_c$  of  $\sim 10$  mm (hence,  $h^* \sim \text{km}$ ) (Lapusta and Rice, 2003; Liu and Rice, 2005).

The grid size  $h$  is chosen such that the cohesive zone  $\Lambda_0 = C_1 \frac{\mu d_c}{(1-\nu)b\bar{\sigma}}$  is at least 3–5 times of  $h$  to ensure continuum during dynamic ruptures (Day et al., 2005; Lapusta and Liu, 2009). Here  $C_1$  is a constant of  $9\pi/32$  for linear shear stress drop (Palmer and Rice, 1973; Lapusta and Liu, 2009). With the theoretical guidelines for the choice of  $h$ , we further conduct three resolution tests with  $h$  of 2 km, 1 km and 0.5 km and run simulations of each case for 200 years to check if they have consistent interseismic and coseismic slip behaviors. As shown in Supplementary Fig. S4, the earthquake occurrence times and afterslip behaviors are quite different using a 2-km grid from those using a 1- or 0.5-km grid, whereas the 1 km and 0.5 km cases have nearly identical velocity history for the first two earthquake cycles. Taking into consideration both the numerical accuracy and computational cost, we consider the 1-km grid size as an optimal choice for our simulation. In total, there are 125,568 triangular elements in the non-planar fault model, which takes about two weeks to complete a 2000-year sequence model using 288 CPU cores on the Compute Canada *Guillimin* HPC cluster.

## 3. Results

Prior to presenting the 3D non-planar fault model findings, we

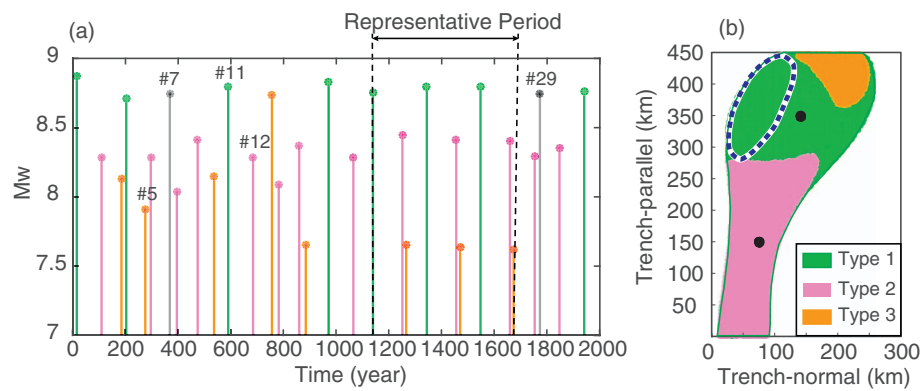


Fig. 3. (a) Simulated 2000-year earthquake sequence on the 3D curved fault. Colors indicate rupture types (Green: whole fault rupture; pink: south segment rupture; orange: north segment rupture; grey: untypical rupture). (b) Rupture areas of earthquakes: Type 1 for whole-fault rupture, Type 2 for partial rupture along the southern segment, and Type 3 for partial rupture along the northern segment, respectively. The blue dashed ellipse: the seismically quiet area as shown in Fig. 2(b). Black dots: map-view locations of the sample areas in Fig. 8, which are 10 km diameter areas located at the middle depth of seismogenic zone along down-dip and respectively at 150 km and 350 km along the strike. (For interpretation of the references to color in this figure legend, the reader is referred to the web version of this article.)

briefly summarize the results from a reference model on a planar fault. For the simulated slip history of 1000 years, all earthquake rupture segmentation occurs at along-strike  $\sim 50$ – $100$  km, further south of the transitional-segment. Detailed results from the planar fault model can be found in the Supporting information (Section S1; Fig. S5). The reference model allows us to make direct comparisons and to assess rupture patterns that are indeed effects of the non-planar fault geometry, instead of being intrinsic to other model parameters.

### 3.1. Modeled earthquake sequences

The maximum moment magnitude of all modeled earthquakes during the 2000-year period is  $\sim M_w 8.8$  (Fig. 3a), comparable to those from the planar fault simulation. The time interval between two  $M_w 8.8$  or greater events ranges from 165 to 220 years, which is more irregular than  $\sim 150$  years from the planar fault model.

Since most events would rupture the entire velocity-weakening zone along the downdip direction, our discussion focuses on the rupture extent along the strike. Here we consider the slip history for  $\sim 400$  years as a representative slip sequence (Fig. 3a). During this period, three types of earthquake ruptures appear in a sequence (see Movie S2 for detailed rupture propagation of the three types of events). Type 1 events typically nucleate either near the transitional-segment or near the southern end of the fault and rupture the entire fault, resulting in magnitudes of  $M_w 8.8$ . In comparison, Type 2 events ( $\sim M_w 8.3$ ) nucleate near the southern end of the fault and propagate across the transitional-segment and terminate  $\sim 50$  km north of it. Type 3 ruptures are smaller, propagating only  $\sim 80$  km locally near the northern end of the fault with an  $M_w$  of 7.8. Furthermore, compared to Types 1 and 2 events that rupture the entire downdip range of the seismogenic zone, Type 3 ruptures are nucleated within the depth range of  $\sim 15$ – $25$  km, while the upper 14 km on the fault remains unruptured. The unruptured segment at along-strike 270–450 km in Types 2 or 3 events (Fig. 3b) also spatially corresponds to the observed seismic gap between  $16.5^\circ\text{N}$ – $19^\circ\text{N}$  (Figs. 1 and 2b). Except for the three rupture types, we observe two untypical ruptures (#7, 29), which nucleate in the north of the transitional-segment, rupture the whole northern segment and stop at the either end of the transitional-segment (Fig. 3a; Movie S2).

### 3.2. Shear stress state and coseismic rupture propagation

The rupture segmentation as illustrated in Fig. 3 can be understood by investigating the shear stress evolution on the fault. Taking a Type 1 event as an example, Fig. 4(a) shows the shear stress distribution on the fault at the beginning of the coseismic phase (defined when maximum slip rate exceeds 5 mm/s) of Event #11 (Fig. 3a). The rupture nucleates at the south and propagates northward. In the southern segment, the contour of the highest shear stresses ( $\sim 34$  MPa; top 15%) in general follows the depth contours between 10 and 20 km; while in the northern segment, the highest shear stress is reached at the upper

$\sim 5$  km depth. Encompassed by the high stress contours are three low stress areas ( $\sim 27$ – $30$  MPa) that respectively correspond to 1) the along-strike range of the transitional-segment, 2) the up-dip of the northern segment ( $\sim 270$ – $420$  km), which also coincides with the seismic gap shown in Figs. 1, and 3) its adjacent down-dip part. The coseismic rupture front, defined by the along-strike position of the most northward element on the largest shear stress rate contour line in each time step, more or less follows the depth contour lines of 10 km in the south and 5 km in the north (Fig. 4b).

Furthermore, the along-strike rupture propagation speed seems to be inversely correlated with the local strike angle of the ‘‘rupture front’’ element, for all the three types of rupture patterns. Here the rupture speed is defined as along-strike propagating speed of the ‘rupture front’, averaged every 25 s. As shown in Fig. 5, for Type 2 event propagating toward the north, the rupture speed gradually decreases as the local strike angle increases in the first  $\sim 150$  km. Further northward propagation is slowed down and eventually stopped at the north side of the transitional-segment ( $\sim 250$  km), following an abrupt increase in the local strike angle from  $\sim 10^\circ$  to nearly  $20^\circ$  at  $\sim 150$  km, a geometrical anomaly related to the subduction of the transitional-segment. Similarly, the rupture propagation speed significantly slows down as a Type 3 event rupture front encounters local strike increases before it eventually stopped at along-strike  $\sim 350$  km (since the rupture propagation of Type 3 event is from north to south, in a reversed sense from that of Type 1 event, the local strike is correspondingly negative). In addition, as the rupture front of the Type 1 event enters the transitional-segment, it takes on a trajectory of a decreasing local strike angle ( $\sim 110$ – $220$  km), different from that of the Type 2 event, such that the rupture manages to continue propagating to the northern boundary of the model domain. Besides such first-order features, the local strike angle is also an effective indication for the small-scale fluctuations in the along-strike rupture speed. For example, the rupture speed of Type 1 event increases with corresponding local strike at  $\sim 250$ – $300$  km, and then decreases as the local strike rises again at  $\sim 300$ – $440$  km.

We further quantify the potential for seismic ruptures to overcome geometrical heterogeneities using the S-ratio (Andrews, 1976):

$$S = \frac{\tau_p - \tau_i}{\tau_i - \tau_r} \quad (4)$$

where  $\tau_p$  is the peak stress,  $\tau_r$  is the residual stress and  $\tau_i$  is the initial shear stress. For each simulated earthquake, we use independent sets of maximum and minimum coseismic shear stresses within the ruptured area to represent  $\tau_p$  and  $\tau_r$  respectively. The initial stress  $\tau_i$  evolves with slip, as calculated from the rate-state friction law, which allows us to investigate the spatial-temporal distribution of the S-ratio. A lower S-ratio implies the initial stress is closer to the peak stress, hence more likely to slip seismically. Within the ruptured area of each earthquake that has nucleated from either side of the 450-km long model domain, we present in Fig. 6 the S-ratios of initial rupture scenarios averaged over every 10-km segment along strike.

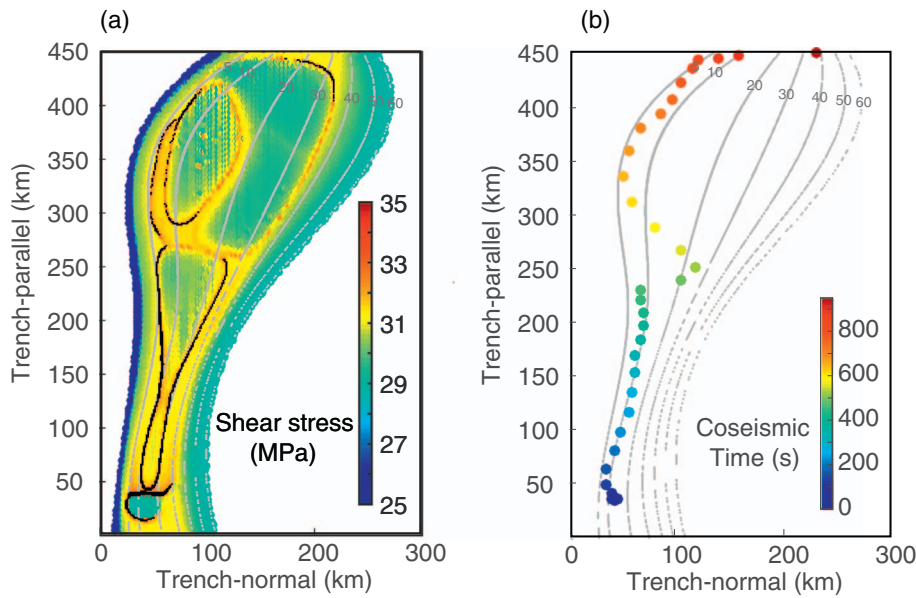


Fig. 4. (a) Shear stress distribution at the initial state of Event #11. Black dots: the highest 15% of shear stress. Grey contours show slab depths. (b) Positions of 'rupture front' of Event #11 in every 25 s.

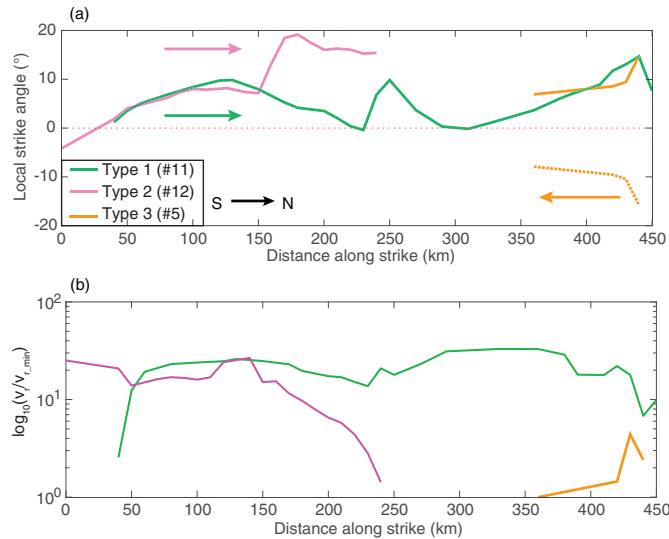


Fig. 5. Comparison between the local strike (a) and the rupture speed (b) for three types of earthquake. Dashed orange curve is the mirror image of the orange curve.

The along-strike variation of S-ratio is generally correlated to the width of seismogenic zone  $W(y)$ . For the rupture direction from south to north, as shown in Fig. 6(a),  $W$  and S-ratio consistently stay stable at the southern segment (~50–200 km), then increase at ~200–370 km segment, and decrease at the northern segment (~370–450 km). Moreover, S-ratio fluctuates along the transitional-segment (~110–220 km), and bifurcates as the gradient of  $W$  reaches largest within the range ~220–300 km. Of the thirteen ruptures shown in Fig. 6(a), only two stop at ~100 km, where  $W$  starts to increase from its minimum (~90 km along-strike). More energetic ruptures do overpass the minimum but six of them eventually stopped as they get close to the segment of the steeply increasing of  $W$  at ~270 km, resulting in Type 2 ruptures as highlighted. Only five events have overcome all the “obstacles”, despite the rise in S-ratios, and continued to rupture all the way to the northern end of the model domain (Type 1). Based on the spatial correlation between the along-strike  $W$  variation and the S-ratio, we infer that an increase in  $W$  may result in larger S ratios (i.e., low pre-stress), which in turn may prohibit rupture propagation. Such patterns can also be inferred for rupture propagations from north to the south (Fig. 6b). S-ratio is much larger for Type 3 events that ruptured along

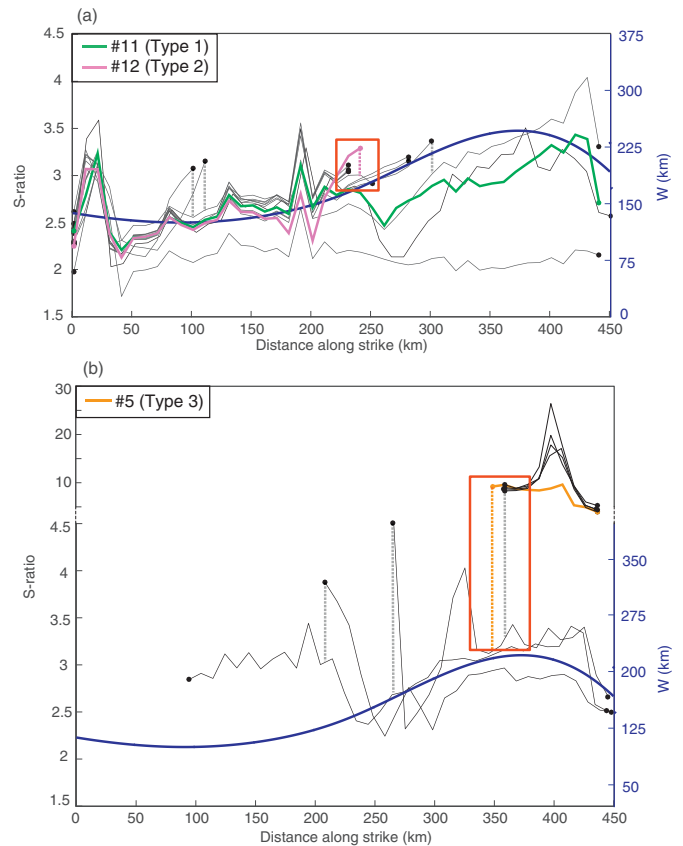


Fig. 6. Comparison between along-strike distribution of seismogenic zone width ( $W$ ) and the S-ratio. (a) Along-strike S-ratio distribution (curves) and rupture termination points (dots) of the initial stage of simulated earthquake sequence ( $v_{max}$  first exceeds 5 mm/s), including Event #11 (green) and #12 (pink). Dotted bars: fluctuation of S-ratio at locations that stop ruptures. Red box: the area where Type 2 ruptures are most frequently terminated. Width of seismogenic zone in a 1-km segment is shown by the thick blue curve. (b) same as (a), except for ruptures propagating from north to south. Event #5 is marked in orange. (For interpretation of the references to color in this figure legend, the reader is referred to the web version of this article.)

the wide northern segment ( $\sim 350\text{--}450\text{ km}$ ) and stopped at the largest  $W$  ( $\sim 350\text{--}370\text{ km}$ ).

Furthermore, S-ratios temporally fluctuate such that at the same along-strike location the S-ratio could be increased over which seismic rupture is prohibited (Fig. 6). Thus, the threshold of S-ratio around rupture terminations could serve as a proxy between the two types of events, i.e., only a smaller S-ratio allows a larger rupture extent. For example, within the range where Type 2 and Type 3 events terminated ( $230\text{--}270\text{ km}$  in Fig. 6a and  $350\text{--}370\text{ km}$  in Fig. 6b), S-ratio thresholds are  $\sim 2.8\text{--}3.2$  and  $\sim 3.0\text{--}10$ , respectively. Considering the S-ratio here is estimated based on the quasi-dynamic modeling, while fully dynamic earthquakes are more likely to propagate through areas with lower pre-stress (larger S-ratio) due to wave-mediated stress transfers, the estimated S-ratio thresholds in this study could be smaller than those from fully dynamic cases.

### 3.3. Comparison between modeling results and seismic observations

For the Manila subduction zone, the accumulative number of interplate earthquakes from 1970 to 2016 clearly exhibits a heterogeneous pattern (Fig. 2b). In the northern Luzon between  $17^\circ\text{N}$  and  $19^\circ\text{N}$  (along-strike  $270\text{--}420\text{ km}$ ) the interplate earthquakes are concentrated at depths of  $\sim 20\text{--}42\text{ km}$  while there is little seismicity in the shallower portion.

Our modeled distribution of interseismic slip rate before Type 1 events (whole-fault rupture) is comparable with the coupling state inferred from such observed seismicity distribution. For instance, Fig. 7 shows the interseismic slip rate on the fault just before a Type 1 event (#11). The fault interface could be mainly divided into three areas, (A) the up-dip area of the seismogenic zone in the north with extremely low interseismic slip rate ( $10^{-6}\text{--}10^{-4}V_{pi}$ ;  $17.5^\circ\text{N}\text{--}19^\circ\text{N}$ ; highlighted in blue dashed lines), (B) the adjacent down-dip area of seismogenic zone in the north ( $10^{-4}\text{--}10^{-3}V_{pi}$ ; yellow dashed lines), and (C) the southern segment with very low interseismic slip rate ( $10^{-5}\text{--}10^{-3}V_{pi}$ ;  $15^\circ\text{N}\text{--}17.5^\circ\text{N}$ ). Apparently area A is firmly locked and later ruptured in

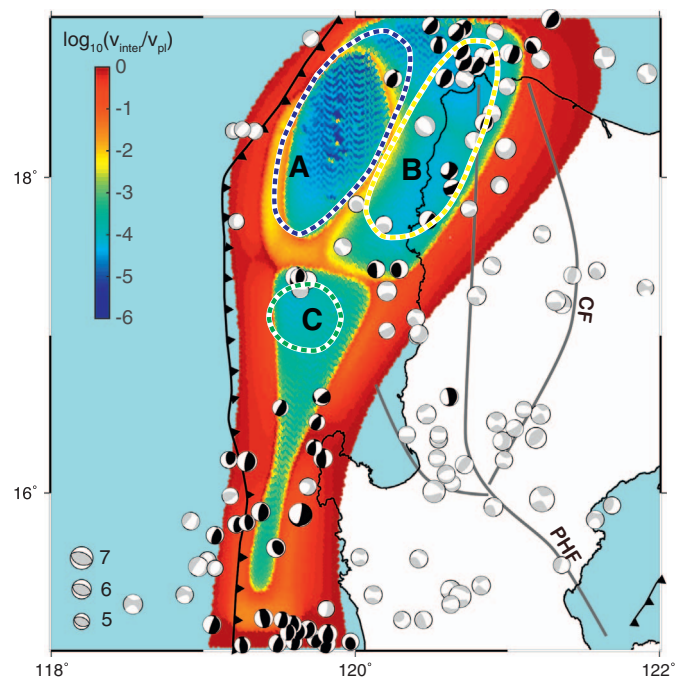


Fig. 7. Comparison between interseismic slip rate (prior to a Type 1 event #11) and the GCMT focal mechanism solutions between 1976/01/01 and 2016/01/01 (<http://www.globalcmt.org>). Black/Grey beachball: interplate/other earthquakes. Blue/Yellow/Green dashed-line circles correspond to Fig. 2(b). (For interpretation of the references to color in this figure legend, the reader is referred to the web version of this article.)

the #11 megathrust earthquake. Note that the area A coincides with the segment lack of interplate earthquakes ( $17^\circ\text{N}\text{--}19^\circ\text{N}$ ; Fig. 2b). In comparison, area B is the transition zone between the highly locked and free-sliding regions, showing much higher interseismic slip rates than those in area A, which may consequently contribute to the active seismicity with moderate magnitudes (Fig. 2b). Area B is also ruptured during Event #11, despite the much smaller slip deficit compared to area A. Area C has an intermediate coupling state manifested by the intermediate slip rates. Earthquakes are similarly distributed on its peripherals where the slip rate is generally higher.

## 4. Discussion

### 4.1. Geometrical effects on shear stress distribution and rupture propagation

Seismic rupture behavior can be affected by many factors, including fault frictional properties (Sibson, 1992), temperature and pressure-controlled rheology (Chen and Molnar, 1983; Hyndman and Wang, 1993), presence of pore fluids (Lockner and Byerlee, 1994; Hillers and Miller, 2007; Liu and Rubin, 2010; Liu, 2013), heterogeneous material distribution across and along the fault (e.g., Mikumo and Miyatake, 1979; Lay et al., 1982; Yang, 2015; Weng et al., 2016), as well as fault topographic features such as subducted seamounts and ridges (e.g., Scholz and Small, 1997; Yang et al., 2013; Wang and Bilek, 2014). Geometrical effects have long been suspected to control rupture segmentation. For instance, two megathrust earthquakes of  $M_w 7.5$  (1996) and  $M_w 8.0$  (2007) along the Peru-Chile Trench have occurred on adjacent segments separated by the Nazca Ridge (Bilek, 2010). The Juan Fernandez Ridge coincides with the southern rupture limit of the 2015  $M_w 8.3$  Illapel, Chile earthquake (Yin et al., 2016), while the Joban seamount chain is suggested to have inhibited the southward propagation of the 2011  $M_w 9.0$  Tohoku-Oki earthquake (Wang and Bilek, 2014). A quantitative investigation of the geometric effect has been conducted by Yang et al. (2013) using a 2D model, whose results indicate that when a seamount (a geometric “bump”) is close to the earthquake nucleation zone it could inhibit rupture propagation with either a higher or lower strength than the neighboring segment. In this study we do not explicitly incorporate the small-scale (1–10 km) geometrical heterogeneities such as a seamount on the subduction fault. Rather, we focus on the large-scale fault topography features ( $\sim 100\text{ km}$ ) and their influences on stress distribution and rupture segmentation. As introduced in Section 3, the differences between slip behavior on the planar and the curved faults are critically influenced by the slab geometry. Unlike the north-south segmentation at along-strike  $\sim 50\text{--}100\text{ km}$  on the planar fault, segmented ruptures nucleate in the south and north on the curved fault and propagation is stopped facing geometrical anomalies (Types 2 and 3). The unruptured area coincides with the observed seismicity gap, and is eventually ruptured in a whole-fault Type 1 event. The apparently contrasting segmentation patterns from the two aforementioned models further confirm that large-scale variations (100 s km) in fault local dip and local strike angles jointly control the shear stress distribution and thus determine the rupture behavior.

We observe in the modeling results that the rupture propagation slows down and eventually stop with an increasing  $W$ , which seems to be contradictory to results based on slip-weakening models. The slip-weakening law and rate- and state- dependent law are essentially the same in governing the slip-weakening behavior during dynamic ruptures (Cocco and Bizzarri, 2002; Bizzarri and Cocco, 2003), which indicates a dynamic failure at the cohesive zone (Ida, 1972; Andrews, 1976). When a marginally steady state (under 2D) has been established, the energy release rate ( $G$ ) near the rupture front is positively related to the width of seismogenic zone, i.e.,  $G \propto \Delta\tau^2 W$ , where  $\Delta\tau$  is the average stress drop (Day, 1982; Weng and Yang, 2017). Given the same initial conditions, a single rupture propagating behavior should be consistent under the framework of these two constitutive laws. Instead of setting a

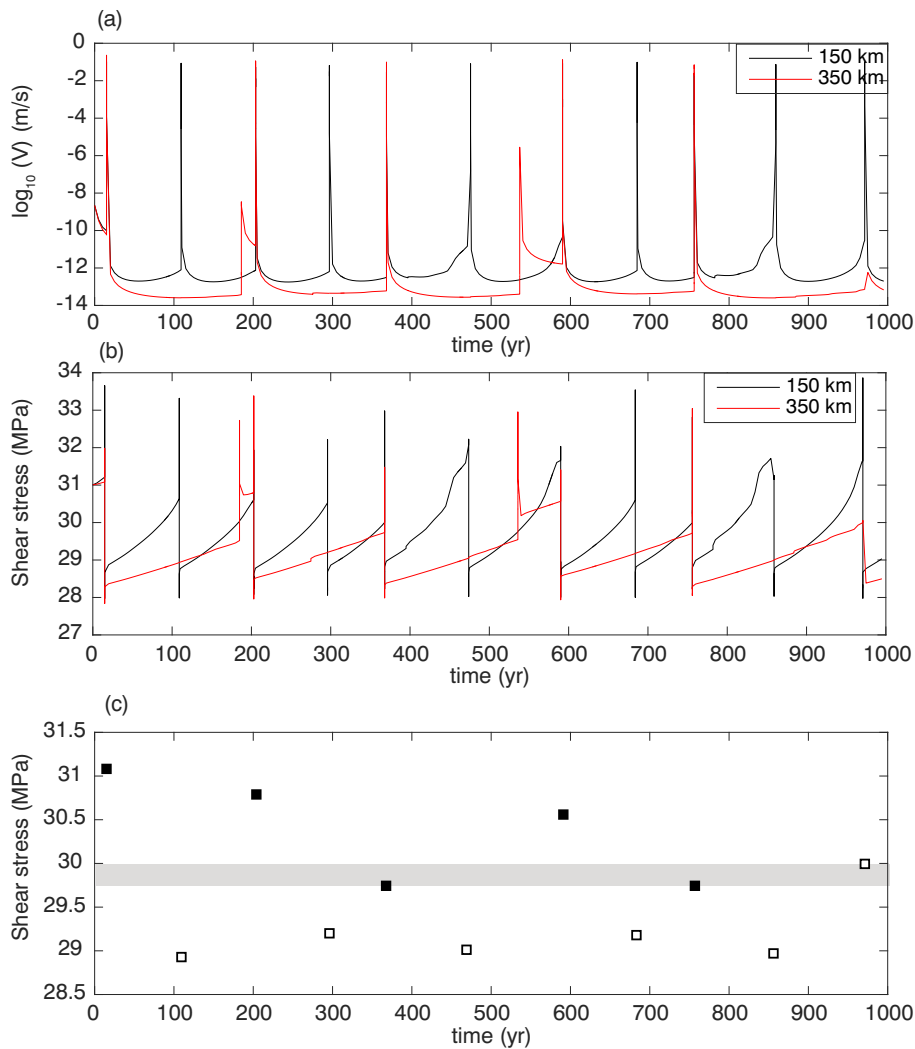


**Fig. 8.** (a) Velocity evolution of sample areas marked in Fig. 3(b). Black/Red curves: evolution of averaged velocity in the southern/northern sample area. (b) The same as (a) but for the shear stress evolution (c) The averaged initial shear stress in the northern sample area corresponding to each rupture on the southern sample. Solid/empty square: the northern sample ruptured/unruptured during the event. The shadow area indicates the threshold stress of coseismic rupture on the northern sample. (For interpretation of the references to color in this figure legend, the reader is referred to the web version of this article.)

uniform shear stress distribution that is critical to rupture in dynamic modeling (Weng and Yang, 2017), we allow the shear stress to evolve during interseismic periods, which is largely affected by the slab geometry (Fig. 4a). After Type 1 events ruptured the whole fault and completely released the slip deficit, the strain energy due to loading should be uniform along strike until the next earthquake (Type 2 events). When the subsequent rupture propagates along the strike, say from  $W_1$  to  $W_2$  ( $W_1 \leq W_2$ ), a total energy conservation requires that  $G(W_1) * W_1 = G(W_2) * W_2$ , which leads to  $G(W_2) = G(W_1) * W_1 / W_2 \leq G(W_1)$ . Therefore, the effective energy release rate is actually reduced as  $W$  increases, which in turn will stop the rupture.

Besides, the evolution of S-ratio/shear stress distribution would further indicate the rupture propagating behavior over earthquake cycles. Here we take two circular patches of 10 km diameter as samples to represent the steeper southern and flatter northern segment (Fig. 3b), and to provide a comparison of the shear stress evolution (Fig. 8). The southern segment has a shorter recurrence period of  $\sim 100$  years and higher interseismic shear stress loading rate  $\sim 20$  kPa/yr compared to the northern one ( $\sim 200$  years;  $\sim 10$  kPa/yr; Figs. 8a-b). The ruptures usually get stopped as  $W$  increases due to the lower shear stress, i.e., higher S-ratio (Types 2 and 3; Fig. 6). Only when the shear stresses on both segments reach  $\sim 30$  MPa or higher, the fault is able to rupture entirely (Type 1; Fig. 8c). The suggested threshold 30 MPa is comparable to the steady-state shear stress at the reference slip rate (Table 1). The S-ratio evolves especially at along-strike locations where ruptures stop ( $\sim 270$  km and 370 km). For example, the rupture termination of

Type 2 events near 220–270 km would introduce high initial stresses to the segment northward, which in turn contributes to a lower S-ratio to facilitate the rupture propagation of the next earthquake. This inter-cycle S-ratio variations may explain the alternating rupture patterns of the three types of events in our simulation (Fig. 6) and reconcile the seemingly paradoxical observations of some earthquake ruptures stopped by seamounts (Kodaira et al., 2000; Cummins et al., 2002) whereas others continuing to propagate forward (Cummins et al., 2002; Duan, 2012).

Earthquake sequences similar to our modeled Types 1–3 events have been observed along the Nankai Trough, southwest Japan. The drastic change of dip angle of the subducting Philippine Sea Plate and strong lateral variation beneath the Kii Peninsula have been suggested to control the rupture segmentation of the 1944 Tonankai (M7.9) and 1946 Nankai (M8.0) earthquakes (Hori et al., 2004; Furumura et al., 2011). The same structural heterogeneity between offshore Shikoku and Mikawa Bay may have also caused the segmentation of the 1854 Ansei Nankai (M8.4) and Ansei Tokai (M8.4) earthquakes, but was ruptured in the 1707 Hiei (M8.4) earthquake (Furumura et al., 2011). Blettery et al. (2016) recently compiled the slab geometry for global subduction zones and found that slab curvature, represented by the along-dip and along-strike gradient in the dip angle, is inversely correlated with the maximum magnitude of earthquakes observed in individual subduction zones. Flat megathrusts tend to have more homogeneous shear stress distribution and hence more favorable for large area ruptures. In our simulation, except for the  $M_w 7.8$  (Type 3) events

that partially rupture the northern edge of the model area, the less steeply dipping northern fault segment with larger seismogenic width takes a longer time to nucleate and is prone to rupture in a whole-fault mega-earthquake (Type 1), while the steeper southern segment with smaller seismogenic width takes a shorter time to nucleate and is ruptured in both whole-fault (Type 1) and segmented ruptures (Type 2). A similar conclusion has been suggested by *Herrendörfer et al. (2015)*, based on qualitative results of 2D subduction earthquake modeling. Our modeling results further indicate along-strike variation of the seismogenic width can influence rupture propagation, which have important implications for interpreting the observed seismicity in the context of interplate coupling state. The spatial correlation between several rupture process properties, either shear stress represented by the S-ratio and the width of seismogenic zone (proportional to the sine of dip angle) or rupture speed and the local strike angle, confirms the strong geometrical effects. For the Manila subduction zone, the Scarborough Seamount Chain is implicitly represented by the transitional-segment in our curved slab model. The drastic along-strike change in fault dip angle related to the subducting seamount chain could be a significant controlling factor in the along-strike rupture segmentation of megathrust earthquakes. Despite the lack of recorded large megathrust earthquakes, our model clearly demonstrates that earthquake rupture segmentation pattern in the Manila subduction zone follows the global trend.

One of the limitations of our modeling is that we do not consider the fault normal stress variations associated with fault geometry. To evaluate the effect of normal stress change, we show an example of  $\Delta\bar{\sigma}$  due to the coseismic slip of a whole-fault earthquake rupture (Type 1 event; Fig. S6). The corresponding static shear stress change is  $\Delta\bar{\sigma} \left[ f_0 + a \ln\left(\frac{v}{v_0}\right) + b \ln\left(\frac{v_0 \theta}{d_c}\right) \right]$ , which is smaller than 1 MPa and not a dominant factor in controlling along-strike rupture propagation compared to the  $\sim 3$  MPa shear stress increasing at the rupture front. Therefore, the ignorance of the spatial variation of  $\bar{\sigma}$  is acceptable for 100 km-scale geometrical topography features in our model; the effect could be more significant at small-scale geometrical anomalies of steeper gradient, as investigated in previous studies (*Dunham et al., 2011; Shi and Day, 2013; Xu and Ben-Zion, 2013*). Future work on this topic needs to quantify the influence of spatial heterogeneities of fault strength introduced by non-uniform normal stress distribution on a nonplanar fault on modeled earthquake rupture sequences. Moreover, to incorporate the temporal variation of  $\bar{\sigma}$  would require considering the frictional memory effects in response to variations in normal stress (*Linker and Dieterich, 1992; Richardson and Marone, 1999; Rice et al., 2001*), which is beyond the scope of this study.

#### 4.2. Estimate of megathrust recurrence interval

The maximum earthquake magnitude recorded in Manila trench area is  $M_w 7.8$  since 1560 (*Repetti, 1946*). However, in our model, the whole fault rupture events (Type 1,  $M_w 8.8$ ) repeat roughly every 200 years, which is much shorter than the average recurrence interval for  $M_w 8.5$  and greater events (*Molnar, 1979; Shimazaki and Nakata, 1980*). The discrepancy may stem from the following simplifications we have made in the simulation.

Firstly, we do not consider the slip and strain partition onto the complex tectonic faults within the Luzon block (e.g., the Philippine Fault, the Cagayan Fault and the Mindoro Fault) (*Zhu et al., 2005*). The full convergence rate of 70 mm/yr is assumed to be trench-normal only and fully contribute to the interplate slip deficit in our model. However, the Luzon segment of the NW-SE striking Philippine Fault, for example, hosts at least seven  $M_w 7+$  earthquakes with a recurrence interval of  $\sim 65$  years, including the  $M_w 7.9$  on July 16, 1990 (*Besana and Ando, 2005*). *Rangin et al. (1999)* estimated the Philippine Fault has accommodated about 55% of the deformation due to subduction, which is supported by more recent GPS observations (*Galgana et al., 2007; Yu*

*et al., 2013*).

Secondly, we set the seismogenic zone as velocity-weakening zone ( $a-b < 0$ ) under the framework of rate and state dependent friction law, in order to investigate the earthquake hazard of the Manila subduction zone. That is, within the seismogenic zone, almost all the plate convergent slip would turn into slip deficit (full locking) and be released coseismically. However, based on the GPS observations, the coupling ratio is suggested to be 0.34–0.48 (*Hsu et al., 2016*). Such overestimation will also proportionally shorten the simulated earthquake interval. In addition, as typical of earthquake sequence models in the framework of the rate-state friction, the generally homogeneous distribution of the frictional stability parameter ( $a-b$ ) in the velocity-weakening zone results in only characteristic earthquakes but no moderate to small magnitude events as on natural tectonic faults (*Liu et al., 2012*). These small-to-moderate magnitude earthquakes would in turn release a fraction of the accumulated strain energy, and hence the estimated large event recurrence time will be biased. Earthquakes of small magnitudes can also be reproduced by introducing small-scale heterogeneities in fault frictional properties or geometry, or the combination of both, or by simply decreasing values of the characteristic slip distance of the friction law (*Lawn, 1993; Lapusta and Rice, 2003; Yang et al., 2012*).

To extrapolate our modeled recurrence interval of  $M_w 8.8$  earthquakes, we take the 55% tectonic deformation and 0.34–0.48 partial coupling ratio (*Hsu et al., 2016*) into consideration, assuming the tectonic movement and the coupling ratio are constant during the interseismic period. Thus, the predicted recurrence interval of  $M_w 8.8$  earthquake could be at least  $200/(1-55\%)/0.48-200/(1-55\%)/0.34$ , i.e., 900–1300 years.

#### 4.3. Earthquake and tsunami hazard in manila subduction zone

Seismicity distribution can be used not only to delineate the extent of the seismogenic zone, but also to infer the locking state on a seismogenic fault (e.g., *Heaton and Kanamori, 1984; Yu et al., 2013*). There are three common interpretations of the relations between seismicity and interseismic fault coupling; (1) repeating earthquakes or aftershocks may indicate creeping of the surrounding fault areas (*Igarashi et al., 2003; Schaff et al., 1998*); (2) microseismicity, some including repeating earthquakes, may also mark the locked-creeping transition (*Beeler et al., 2001; Sammis and Rice, 2001; Pandey et al., 1995, 1999*); (3) seismic quiescence indicates either extensively locked fault (*Wyss and Habermann, 1988; Fialko, 2006*) or aseismically slipping (*Ando and Balazs, 1979*). If the distribution of the present-day seismicity in the Manila subduction zone reflects the stress state before Type 1 ruptures in our model, our results suggest that the northern seismic gap area of the Manila trench is possibly accumulating strain energy and would be capable of rupturing in a  $M 8+$  megathrust earthquake in the future. The verification of the inferred slip deficit with geodetic measurements along the margin is challenging due to the limited coverage in space and in time and uncertainties in the different inversion algorithms (*Galgana et al., 2007; Hsu et al., 2012; McCaffrey, 2002; Wang and Tréhu, 2016*). Moreover, as clearly illustrated in Fig. 7, all the strongly locked fault segments are located offshore, which requires future sea-floor geodesy to scrutinize the nature of the seismic gap in the northern Luzon.

Our geometrical effects-imbedded rupture model indicates that during a whole-fault rupture (Type 1), the coseismic slip along the northern fault segment is much larger than the southern, and therefore suggests that 1) the corresponding tsunami hazard along the west coast of Luzon island varies from the south to north. The segment of  $\sim 18^\circ\text{N}-19^\circ\text{N}$  may expect the strongest hit; 2) tsunami hazard may be underestimated along the coast of southwest Taiwan. The run-up amplitude there could be comparable to that along southeast China, based on a preliminary tsunami simulation taking the simulated  $M_w 8.8$  coseismic slip distribution, rather than 1/3 in the previous studies (*Megawati*

et al., 2009). Considering the population density in these areas is as high as  $10^2$ – $10^4$  persons/km<sup>2</sup>, our rupture model here might be significant to stress the tsunami hazard in the northeast region of the South China sea.

## 5. Conclusions

We conduct numerical simulations of earthquake rupture sequences in the framework of rate- and state-dependent friction law along the 15°N–19°N segment of the Manila Trench, South China Sea, to assess the potential of  $M_w$ 8+ megathrust earthquakes along the subduction zone. The three-dimensional non-planar subduction fault geometry is approximated from earthquake hypocenters and illustrates strong variations in fault dip and strike angles around 16°N–17°N (transitional-segment), presumably due to the subducting Scarborough Seamount Chain (SSC). Our modeling results demonstrate that the down-dip width of seismogenic zone  $W$  controls megathrust earthquake rupture patterns to the first-order. Fault shear stress evolution, represented by the  $S$ -ratio, clearly follows the distribution of  $W$ . A large  $W$  indicates longer rupture recurrence period because of lower interseismic stress loading rate, and could slow down or sometimes stop ruptures due to its lower shear stress state. The strong fault curvature between 16°N–17°N typically segments ruptures to the south and north ( $M_w$ 8.3 and  $M_w$ 7.8, Type 2 and 3 events respectively), and occasionally experiences seismic slip in  $M_w$ 8.8 whole-fault ruptures (Type 1 events) when the cumulative stress in the transitional-segment is high enough to overcome the geometrical inhibition. The rupture propagating speed, although under the quasi-dynamic approximation, is inversely correlated with the fault local strike angle.

Our modeling results also demonstrate a spatial correlation between interseismic coupling state before a whole-fault rupture (Type 1) and observed seismicity along the Manila Trench. The unruptured area between Types 2 and 3 events corresponds to a segment of low seismicity rate. Recorded  $M7$  or smaller interplate earthquakes in general occur on the peripherals of the simulated strongly coupled areas during the interseismic period, suggesting that  $M8+$  earthquakes can potentially nucleate and rupture along the Manila Trench.

Supplementary data to this article can be found online at <https://doi.org/10.1016/j.tecto.2018.01.025>.

## Acknowledgments

H. Yu is supported by the Natural Sciences and Engineering Research Council of Canada Discovery Grant (NSERC RGPIN 418338-12) and the Fonds de recherche du Québec-Nature et technologies Team Grant (FRQNT PR-191259) to Y. Liu at McGill University. H. Yang is supported by Faculty of Science at the Chinese University of Hong Kong, HKSAR Research Grant Council ECS Grant 24601515 and GRF Grant 14313816, and NSFC/RGC Joint Research Scheme (Project No. N\_CUHK430/16). J. Ning is supported by The China Seismic Array Program under Grants DQJB16A0307 and DQJB17A0103. We are grateful to B. Shibasaki, and T. Matsuzawa, who kindly shared the codes for triangular mesh generating and for calculating the kernels for a triangular element. We use the server Guillimin of Compute Canada at McGill University.

## References

Ando, M., Balazs, E.I., 1979. Geodetic evidence for aseismic subduction of the Juan de Fuca plate. *J. Geophys. Res. Solid Earth* 84 (B6), 3023–3028.

Andrews, D.J., 1976. Rupture velocity of plane strain shear cracks. *J. Geophys. Res.* 81 (32), 5679–5687. <http://dx.doi.org/10.1029/JB081i032p05679>.

Bautista, M.L.P., Oike, K., 2000. Estimation of the magnitudes and epicenters of Philippine historical earthquakes. *Tectonophysics* 317 (1), 137–169. [http://dx.doi.org/10.1016/S0040-1951\(99\)00272-3](http://dx.doi.org/10.1016/S0040-1951(99)00272-3).

Bautista, B.C., Bautista, M.L.P., Oike, K., Wu, F.T., Punongbayan, R.S., 2001. A new insight on the geometry of subducting slabs in northern Luzon, Philippines. *Tectonophysics* 339 (3), 279–310. [http://dx.doi.org/10.1016/S0040-1951\(01\)](http://dx.doi.org/10.1016/S0040-1951(01)00120-2)

00120-2.

Beeler, N.M., Lockner, D.L., Hickman, S.H., 2001. A simple stick-slip and creep-slip model for repeating earthquakes and its implication for microearthquakes at Parkfield. *Bull. Seismol. Soc. Am.* 91 (6), 1797–1804.

Besana, G.M., Ando, M., 2005. The central Philippine fault zone: location of great earthquakes, slow events and creep activity. *Earth Planets Space* 57 (10), 987–994. <http://dx.doi.org/10.1186/BF03351877>.

Bilek, S.L., 2010. Invited review paper: seismicity along the South American subduction zone: review of large earthquakes, tsunamis, and subduction zone complexity. *Tectonophysics* 495 (1), 2–14. <http://dx.doi.org/10.1016/j.tecto.2009.02.037>.

Bizzarri, A., Cocco, M., 2003. Slip-weakening behavior during the propagation of dynamic ruptures obeying rate-and state-dependent friction laws. *J. Geophys. Res. Solid Earth* 108 (B8). <http://dx.doi.org/10.1029/2002JB002198>.

Blanpied, M.L., Lockner, D.A., Byerlee, J.D., 1995. Frictional slip of granite at hydrothermal conditions. *J. Geophys. Res. Solid Earth* 100 (B7), 13045–13064. <http://dx.doi.org/10.1029/95JB00862>.

Bletery, Q., Thomas, A.M., Rempel, A.W., Karlstrom, L., Sladen, A., De Barros, L., 2016. Mega-earthquakes rupture flat megathrusts. *Science* 354 (6315), 1027–1031. <http://dx.doi.org/10.1126/science.aag0482>.

Chen, W.P., Molnar, P., 1983. Focal depths of intracontinental and intraplate earthquakes and their implications for the thermal and mechanical properties of the lithosphere. *J. Geophys. Res. Solid Earth* 88 (B5), 4183–4214. <http://dx.doi.org/10.1029/JB088iB05p04183>.

Cocco, M., Bizzarri, A., 2002. On the slip-weakening behavior of rate-and state dependent constitutive laws. *Geophys. Res. Lett.* 29 (11). <http://dx.doi.org/10.1029/2001GL013999>.

Cummins, P.R., Baba, T., Kodaira, S., Kaneda, Y., 2002. The 1946 Nankai earthquake and segmentation of the Nankai Trough. *Phys. Earth Planet. Inter.* 132 (1), 75–87. [http://dx.doi.org/10.1016/S0031-9201\(02\)00045-6](http://dx.doi.org/10.1016/S0031-9201(02)00045-6).

Day, S., 1982. Three-dimensional finite difference simulation of fault dynamics: rectangular faults with fixed rupture velocity. *Bull. Seismol. Soc. Am.* 72 (3), 705–727.

Day, S.M., Dalguer, L.A., Lapusta, N., Liu, Y., 2005. Comparison of finite difference and boundary integral solutions to three-dimensional spontaneous rupture. *J. Geophys. Res. Solid Earth* 110 (B12).

Dieterich, J.H., 1979. Modeling of rock friction: 1. Experimental results and constitutive equations. *J. Geophys. Res.* 84, 2161–2168. <http://dx.doi.org/10.1029/JB084iB05p02161>.

Duan, B., 2012. Dynamic rupture of the 2011 Mw 9.0 Tohoku-Oki earthquake: roles of a possible subducting seamount. *J. Geophys. Res. Solid Earth* 117 (B5). <http://dx.doi.org/10.1029/2011JB009124>.

Dunham, E., Belanger, D., Cong, L., Kozdon, J., 2011. Earthquake ruptures with strong rate-weakening friction and off-fault plasticity, part 2: nonplanar faults. *Bull. Seismol. Soc. Am.* 101 (5), 2308–2322. <http://dx.doi.org/10.1785/0120100076>.

Fan, J.K., Wu, S.G., 2014. P-wave seismic tomography of the Manila subduction zone. *Chin. J. Geophys.* 57 (7), 2127–2137. (in Chinese). <https://doi.org/10.6038/cjg20140709>.

Fialko, Y., 2006. Interseismic strain accumulation and the earthquake potential on the southern San Andreas fault system. *Nature* 441 (7096), 968.

Furumura, T., Imai, K., Maeda, T., 2011. A revised tsunami source model for the 1707 Hoei earthquake and simulation of tsunami inundation of Ryujin Lake, Kyushu, Japan. *J. Geophys. Res. Solid Earth* 116 (B2). <http://dx.doi.org/10.1029/2010JB007918>.

Galgana, G., Hamburger, M., McCaffrey, R., Corpuz, E., 2007. Analysis of crustal deformation in Luzon, Philippines using geodetic observations and earthquake focal mechanisms. *Tectonophysics* 432 (1–4), 63–87. <http://dx.doi.org/10.1016/j.tecto.2006.12.001>.

Gao, X., Zhang, J., Sun, Y.J., Wu, S.G., 2012. A simulation study on the thermal structure of Manila Trench subduction zone. *Chin. J. Geophys.* 55 (1), 35–45. <http://dx.doi.org/10.1002/cjg2.1698>.

He, C., Wang, Z., Yao, W., 2007. Frictional sliding of gabbro gouge under hydrothermal conditions. *Tectonophysics* 445 (3), 353–362. <http://dx.doi.org/10.1016/j.tecto.2007.09.008>.

Heaton, T.H., Kanamori, H., 1984. Seismic potential associated with subduction in the northwestern United States. *Bull. Seismol. Soc. Am.* 74 (3), 933–941.

Herrendorf, R., van Dinther, Y., Gerya, T., Dalguer, L.A., 2015. Earthquake supercycle in subduction zones controlled by the width of the seismogenic zone. *Nat. Geosci.* 8 (6), 471–474. <http://dx.doi.org/10.1038/ngeo2427>.

Hillers, G., Miller, S.A., 2007. Dilatancy controlled spatiotemporal slip evolution of a sealed fault with spatial variations of the pore pressure. *Geophys. J. Int.* 168 (1), 431–445. <http://dx.doi.org/10.1111/j.1365-246X.2006.03167.x>.

Hori, T., Kato, N., Hirahara, K., Baba, T., Kaneda, Y., 2004. A numerical simulation of earthquake cycles along the Nankai Trough in southwest Japan: lateral variation in frictional property due to the slab geometry controls the nucleation position. *Earth Planet. Sci. Lett.* 228 (3), 215–226 (doi:10.1016/j.epsl.2004.09.033).

Hsu, Y.J., Yu, S.B., Song, T.R.A., Bacolcol, T., 2012. Plate coupling along the Manila subduction zone between Taiwan and northern Luzon. *J. Asian Earth Sci.* 51, 98–108. <http://dx.doi.org/10.1016/j.jseas.2012.01.005>.

Hsu, Y.J., Yu, S.B., Loveless, J.P., Bacolcol, T., Solidum, R., Luis, A., Pelicano, A., Woessner, J., 2016. Interseismic deformation and moment deficit along the Manila subduction zone and the Philippine Fault system. *J. Geophys. Res. Solid Earth* 121 (10), 7639–7665. <http://dx.doi.org/10.1002/2016JB013082>.

Hyndman, R.D., Wang, K., 1993. Thermal constraints on the zone of major thrust earthquake failure: the Cascadia subduction zone. *J. Geophys. Res. Solid Earth* 98 (B2), 2039–2060. <http://dx.doi.org/10.1029/92JB02279>.

Ida, Y., 1972. Cohesive force across the tip of a longitudinal-shear crack and Griffith's specific surface energy. *J. Geophys. Res.* 77 (20), 3796–3805.

- Igarashi, T., Matsuzawa, T., Hasegawa, A., 2003. Repeating earthquakes and interplate aseismic slip in the northeastern Japan subduction zone. *J. Geophys. Res. Solid Earth* 108 (B5).
- Kaneko, Y., Avouac, J.P., Lapusta, N., 2010. Towards inferring earthquake patterns from geodetic observations of interseismic coupling. *Nat. Geosci.* 3 (5), 363–369. <http://dx.doi.org/10.1038/ngeo843>.
- King, G.C.P., 1986. Speculations on the geometry of the initiation and termination process of earthquake rupture and its relation to morphology and geological structure. *Pure Appl. Geophys.* 124 (3), 567–585.
- Kodaira, S., Takahashi, N., Nakanishi, A., Miura, S., Kaneda, Y., 2000. Subducted seamount imaged in the rupture zone of the 1946 Nankaido earthquake. *Science* 289 (5476), 104–106. <http://dx.doi.org/10.1126/science.289.5476.104>.
- Lapusta, N., Liu, Y., 2009. Three-dimensional boundary integral modeling of spontaneous earthquake sequences and aseismic slip. *J. Geophys. Res. Solid Earth* 114 (B9), 2156–2202.
- Lapusta, N., Rice, J.R., 2003. Nucleation and early seismic propagation of small and large events in a crustal earthquake model. *J. Geophys. Res.* 108 (B4), 2205. <http://dx.doi.org/10.1029/2001JB000793>.
- Lapusta, N., Rice, J.R., Ben-Zion, Y., Zheng, G., 2000. Elastodynamic analysis for slow tectonic loading with spontaneous rupture episodes on faults with rate- and state-dependent friction. *J. Geophys. Res. Solid Earth* 105 (B10), 23765–23789.
- Lawn, B., 1993. *Fracture of Brittle Solids*, 2nd edition. Cambridge Univ. Press, Cambridge.
- Lay, T., 2015. The surge of great earthquakes from 2004 to 2014. *Earth Planet. Sci. Lett.* 409, 133–146. <http://dx.doi.org/10.1016/j.epsl.2014.10.047>.
- Lay, T., Kanamori, H., Ruff, L., 1982. The asperity model and the nature of large subduction zone earthquakes. *Earthq. Prediction Res.* 1 (1), 3–71.
- Li, D., Liu, Y., 2016. Spatiotemporal evolution of slow slip events in a nonplanar fault model for northern Cascadia subduction zone. *J. Geophys. Res. Solid Earth* 121 (9), 6828–6845. <http://dx.doi.org/10.1002/2016JB012857>.
- Linker, M.F., Dieterich, J.H., 1992. Effects of variable normal stress on rock friction: Observations and constitutive equations. *J. Geophys. Res. Solid Earth* 97 (B4), 4923–4940.
- Liu, Y., 2013. Numerical simulations on megathrust rupture stabilized under strong dilatancy strengthening in slow slip region. *Geophys. Res. Lett.* 40 (7), 1311–1316. <http://dx.doi.org/10.1002/grl.50298>.
- Liu, Y., Rice, J.R., 2005. Aseismic slip transients emerge spontaneously in three-dimensional rate and state modeling of subduction earthquake sequences. *J. Geophys. Res.* 110, B08307. <http://dx.doi.org/10.1029/2004JB003424>.
- Liu, Y., Rice, J.R., 2009. Slow slip predictions based on granite and gabbro friction data compared to GPS measurements in northern Cascadia. *J. Geophys. Res. Solid Earth* 114, B09407. <http://dx.doi.org/10.1029/2008JB006142>.
- Liu, Y., Rubin, A.M., 2010. Role of fault gouge dilatancy on aseismic deformation transients. *J. Geophys. Res. Solid Earth* 115, B10414. <http://dx.doi.org/10.1029/2010JB007522>.
- Liu, Y., Santos, A., Wang, S.M., Shi, Y., Liu, H., Yuen, D.A., 2007. Tsunami hazards along Chinese coast from potential earthquakes in South China Sea. *Phys. Earth Planet. Inter.* 163 (1), 233–244.
- Liu, P.L., Wang, X., Solisburly, A.J., 2009. Tsunami hazard and forecast study in South China Sea. *J. Asian Earth Sci.* 36 (1), 2–12.
- Liu, Y., McGuire, J.J., Behn, M.D., 2012. Frictional behavior of oceanic transform faults and its influence on earthquake characteristics. *J. Geophys. Res. Solid Earth* 117, B04315. <http://dx.doi.org/10.1029/2011JB009025>.
- Lockner, D.A., Byerlee, J.D., 1994. Dilatancy in hydraulically isolated faults and the suppression of instability. *Geophys. Res. Lett.* 21 (22), 2353–2356. <http://dx.doi.org/10.1029/94GL02366>.
- McCaffrey, R., 2002. Crustal Block Rotations and Plate Coupling. *Plate Boundary Zones*, pp. P101–122. <http://dx.doi.org/10.1029/GD030p0101>. (Copyright 2002 by the American Geophysical Union).
- McCaffrey, R., 2008. Global frequency of magnitude 9 earthquakes. *Geology* 36 (3), 263–266. <http://dx.doi.org/10.1130/G24402A.1>. (Mar 1).
- Megawati, K., Shaw, F., Sieh, K., Huang, Z., Wu, T.R., Lin, Y., ... Pan, T.C., 2009. Tsunami hazard from the subduction megathrust of the South China Sea: part I. Source characterization and the resulting tsunami. *J. Asian Earth Sci.* 36 (1), 13–20. <http://dx.doi.org/10.1016/j.jseae.2008.11.012>.
- Mikumo, T., Miyatake, T., 1979. Earthquake sequences on a frictional fault model with non-uniform strengths and relaxation times. *Geophys. J. Int.* 59 (3), 497–522.
- Miller, M.M., Johnson, D.J., Rubin, C.M., Dragert, H., Wang, K., Qamar, A., Goldfinger, C., 2001. GPS-determination of along-strike variation in Cascadia margin kinematics: implications for relative plate motion, subduction zone coupling, and permanent deformation. *Tectonics* 20 (2), 161–176. <http://dx.doi.org/10.1029/2000TC001224>.
- Molnar, P., 1979. Earthquake recurrence intervals and plate tectonics. *Bull. Seismol. Soc. Am.* 69 (1), 115–133.
- Nishimura, T., Hirasawa, T., Miyazaki, S.I., Sagiya, T., Tada, T., Miura, S., Tanaka, K., 2004. Temporal change of interplate coupling in northeastern Japan during 1995–2002 estimated from continuous GPS observations. *Geophys. J. Int.* 157 (2), 901–916. <http://dx.doi.org/10.1111/j.1365-246X.2004.02159.x>.
- Okada, Y., 1992. Internal deformation due to shear and tensile faults in a half-space. *Bull. Seismol. Soc. Am.* 82 (2), 1018–1040.
- Palmer, A.C., Rice, J.R., 1973. The growth of slip surfaces in the progressive failure of over-consolidated clay. In: *Proceedings of the Royal Society of London A: Mathematical, Physical and Engineering Sciences*. Vol. 332, No. 1591. The Royal Society, pp. 527–548 (Apr 3).
- Pandey, M., Tankadar, R., Avouac, J.-P., Lavé, J., Massot, J.-P., 1995. Interseismic strain accumulation on the Himalayan crustal ramp (Nepal). *Geophys. Res. Lett.* 22, 751–754.
- Pandey, M., Tankadar, R., Avouac, J.-P., Vergne, J., Héritier, T., 1999. Seismotectonics of the Nepal Himalaya from a local seismic network. *J. Asian Earth Sci.* 17, 703–712.
- Rangin, C., Le Pichon, X., Mazzotti, S., Pubellier, M., Chamot-Rooke, N., Aurelio, M., ... Quebral, R., 1999. Plate convergence measured by GPS across the Sundaland/Philippine Sea plate deformed boundary: the Philippines and eastern Indonesia. *Geophys. J. Int.* 139 (2), 296–316. <http://dx.doi.org/10.1046/j.1365-246x.1999.00969.x>.
- Repetti, W.C., 1946. Catalogue of Philippine earthquakes, 1589–1899. *Bull. Seismol. Soc. Am.* 36 (3), 133–322.
- Reyners, M., 1998. Plate coupling and the hazard of large subduction thrust earthquakes at the Hikurangi subduction zone, New Zealand. *N. Z. J. Geol. Geophys.* 41 (4), 343–354. <http://dx.doi.org/10.1080/00288306.1998.9514815>.
- Rice, J.R., 1992. Fault stress states, pore pressure distributions, and the weakness of the San Andreas fault. *International. Geophysics* 51, 475–503. [http://dx.doi.org/10.1016/S0074-6142\(08\)62835-1](http://dx.doi.org/10.1016/S0074-6142(08)62835-1).
- Rice, J.R., 1993. Spatiotemporal complexity of slip on a fault. *J. Geophys. Res.* 98 (B6), 9885–9907. <http://dx.doi.org/10.1029/93JB00191>.
- Rice, J.R., Lapusta, N., Ranjith, K., 2001. Rate and state dependent friction and the stability of sliding between elastically deformable solids. *J. Mech. Phys. Solids* 49 (9), 1865–1898.
- Richardson, E., Marone, C., 1999. Effects of normal stress vibrations on frictional healing. *J. Geophys. Res. Solid Earth* 104 (B12), 28859–28878.
- Ruina, A.L., 1983. Slip instability and state variable friction laws. *J. Geophys. Res.* 88 (10), 359–10,370. <http://dx.doi.org/10.1029/JB088iB12p10359>.
- Saffer, D.M., Tobin, H.J., 2011. Hydrogeology and mechanics of subduction zone forearc: fluid flow and pore pressure. *Annu. Rev. Earth Planet. Sci.* 39 (2011), 157–186.
- Sammis, C.G., Rice, J.R., 2001. Repeating earthquakes as low-stress-drop events at a border between locked and creeping fault patches. *Bull. Seismol. Soc. Am.* 91 (3), 532–537.
- Schaff, D.P., Beroza, G.C., Shaw, B.E., 1998. Postseismic response of repeating aftershocks. *Geophys. Res. Lett.* 25 (24), 4549–4552. <http://dx.doi.org/10.1029/1998GL900192>.
- Scholz, C.H., Campos, J., 2012. The seismic coupling of subduction zones revisited. *J. Geophys. Res.* 117 (B5), 2156–2202. <http://dx.doi.org/10.1029/2011JB009003>.
- Scholz, C.H., Small, C., 1997. The effect of seamount subduction on seismic coupling. *Geology* 25 (6), 487–490.
- Shi, Z., Day, S.M., 2013. Rupture dynamics and ground motion from 3-D rough-fault simulations. *J. Geophys. Res. Solid Earth* 118, 1122–1141. <http://dx.doi.org/10.1002/jgrb.50094>.
- Shibazaki, B., Obara, K., Matsuzawa, T., Hirose, H., 2012. Modeling of slow slip events along the deep subduction zone in the Kii Peninsula and Tokai regions, southwest Japan. *J. Geophys. Res.* 117, B06311. <http://dx.doi.org/10.1029/2011JB009083>.
- Shimazaki, K., Nakata, T., 1980. Time-predictable recurrence model for large earthquakes. *Geophys. Res. Lett.* 7 (4), 279–282. <http://dx.doi.org/10.1029/GL007i004p0279>.
- Sibson, R.H., 1992. Implications of fault-valve behaviour for rupture nucleation and recurrence. *Tectonophysics* 211 (1–4), 283–293. [http://dx.doi.org/10.1016/0040-1951\(92\)90065-E](http://dx.doi.org/10.1016/0040-1951(92)90065-E).
- Stuart, W., Hildenbrand, T., Simpson, R., 1997. Stressing of the New Madrid seismic zone by a lower crust detachment fault. *J. Geophys. Res. Solid Earth* 102 (B12), 27623–27633. <http://dx.doi.org/10.1029/97JB02716>. (Dec 10).
- Thomas, M.Y., Lapusta, N., Noda, H., Avouac, J.-P., 2014. Quasi-dynamic versus fully dynamic simulations of earthquakes and aseismic slip with and without enhanced coseismic weakening. *J. Geophys. Res. Solid Earth* 119, 1986–2004. <http://dx.doi.org/10.1002/2013JB010615>.
- Wang, K., Bilek, S., 2014. Invited review paper: fault creep caused by subduction of rough seafloor relief. *Tectonophysics* 610, 1–24. <http://dx.doi.org/10.1016/j.tecto.2013.11.024>.
- Wang, K., Tréhu, A.M., 2016. Invited review paper: some outstanding issues in the study of great megathrust earthquakes—the Cascadia example. *J. Geodyn.* 98, 1–18. <http://dx.doi.org/10.1016/j.jog.2016.03.010>.
- Weng, H., Yang, H., 2017. Seismogenic width controls aspect ratios of earthquake ruptures. *Geophys. Res. Lett.* 44 (6), 2725–2732. <http://dx.doi.org/10.1002/2016GL072168>.
- Weng, H., Yang, H., Zhang, Z., Chen, X., 2016. Earthquake rupture extents and coseismic slips promoted by damaged fault zones. *J. Geophys. Res.* 121 (6), 4446–4457. <http://dx.doi.org/10.1002/2015JB012713>.
- Wessel, P., Bercovici, D., 1998. Interpolation with splines in tension: a Green's function approach. *Math. Geol.* 30 (1), 77–93. <http://dx.doi.org/10.1023/A:1021713421882>.
- Wu, T.R., Huang, H.C., 2009. Modeling tsunami hazards from Manila trench to Taiwan. *J. Asian Earth Sci.* 36 (1), 21–28. <http://dx.doi.org/10.1016/j.jseae.2008.12.006>.
- Wyss, M., Habermann, R.E., 1988. Precursory seismic quiescence. *Pure Appl. Geophys.* 126 (2), 319–332.
- Xu, S., Ben-Zion, Y., 2013. Numerical and theoretical analyses of in-plane dynamic rupture on a frictional interface and off-fault yielding patterns at different scales. *Geophys. J. Int.* Vol. 193 (1), 304–320. <http://dx.doi.org/10.1093/gji/ggs105>. (1 April 2013).
- Yang, H., 2015. Recent advances in imaging crustal fault zones: a review. *Earthq. Sci.* 28, 151–162. <http://dx.doi.org/10.1007/s11589-015-0114-3>.
- Yang, M., Wei, B., 2005. The potential seismic tsunami risk in South China Sea and its surrounding region. *J. Catastrophol.* 20, 41–47 (in Chinese with English abstract).
- Yang, H., Liu, Y., Lin, J., 2012. Effects of subducted seamounts on megathrust earthquake nucleation and rupture propagation. *Geophys. Res. Lett.* 39 (24), L24302. <http://dx.doi.org/10.1029/2012GL053892>.
- Yang, H., Liu, Y., Lin, J., 2013. Geometrical effects of a subducted seamount on stopping megathrust ruptures. *Geophys. Res. Lett.* 40 (10), 2011–2016. <http://dx.doi.org/10.1002/grl.50509>.

- Yin, J., Yang, H., Yao, H., Weng, H., 2016. Coseismic radiation and stress drop during the 2015 Mw 8.3 Illapel, Chile megathrust earthquake. *Geophys. Res. Lett.* 43, 1520–1528. <http://dx.doi.org/10.1002/2015GL067381>.
- Yu, S.B., Kuo, L.C., Punongbayan, R.S., Ramos, E.G., 1999. GPS observation of crustal deformation in the Taiwan-Luzon. *Geophys. Res. Lett.* 26 (7), 923–926. <http://dx.doi.org/10.1029/1999GL900148>.
- Yu, H.Y., Tao, K., Cai, C., Zhang, H., Ning, J.Y., Wang, Y.B., 2013. Focal mechanism solutions of the tohoku-Oki earthquake sequence and their geodynamical implications. *Chin. J. Geophys.* 56 (8), 2655–2669. <http://dx.doi.org/10.6038/cjg20130815>.
- Zhu, J.J., Qiu, X.L., Zhan, W.H., Xu, H.L., Sun, L.T., 2005. Focal mechanism solutions and its tectonic significance in the trench of the eastern South China Sea. *Acta Seismol. Sin.* 18 (3), 280–289. <http://dx.doi.org/10.1007/s11589-005-0076-y>.